This is an open access article published under an ACS AuthorChoice License, which permits copying and redistribution of the article or any adaptations for non-commercial purposes.

ACS central science

Research Article

Cite This: ACS Cent. Sci. 2019, 5, 1044−1058

http://pubs.acs.org/journal/acscii

Thermal-Responsive Carbon Monoxide (CO) Delivery Expedites Metabolic Exhaustion of Cancer Cells toward Reversal of Chemotherapy Resistance

Yongjuan Li, Juanjuan Dang, Qiujun Liang, and Lichen Yin*

Institute of Functional Nano and Soft Materials (FUNSOM), Jiangsu Key Laboratory for Carbon-Based Functional Materials and Devices, Collaborative Innovation Center of Suzhou Nano Science and Technology, Soochow University, Suzhou 215123, China

Supporting Information

ABSTRACT: Multidrug resistance (MDR) is the main cause of chemotherapy failure, and the mechanism of MDR is largely associated with drug efflux mediated by the adenosine triphosphate (ATP)-binding cassette transporters. Herein, an NIR-light-triggered CO release system based on mesoporous Prussian blue nanoparticles (PB NPs) was developed to reverse MDR via CO-induced metabolic exhaustion. Pentacarbonyl iron ($Fe(CO)_5$) as the CO producer was coupled to PB NPs via coordination interaction, and doxorubicin (Dox) was encapsulated into the pores of PB NPs. After layer-by-layer (LBL) coating, the NPs showed desired serum stability to enhance tumor accumulation. Upon tumor-site-specific NIR light (808 nm) irradiation, the nonlethal temperature elevation cleaved the Fe−CO bond to release CO. CO then expedited mitochondrial metabolic exhaustion to block ATP synthesis and inhibit ATP-dependent drug efflux, thus reversing MDR of the Dox-resistant MCF-7/ADR tumors to potentiate the anticancer efficacy of Dox. In the meantime, CO-mediated mitochondrial exhaustion could upregulate the proapoptotic protein, caspase 3, thus inducing cellular apoptosis and enabling a synergistic anticancer effect with chemotherapy. To the best of our knowledge, this is the first time MDR has been overcome using a CO delivery system. This study provides a promising strategy to realize an effective and safe treatment against MDR tumors and reveals new insights in the use of CO for cancer treatment.

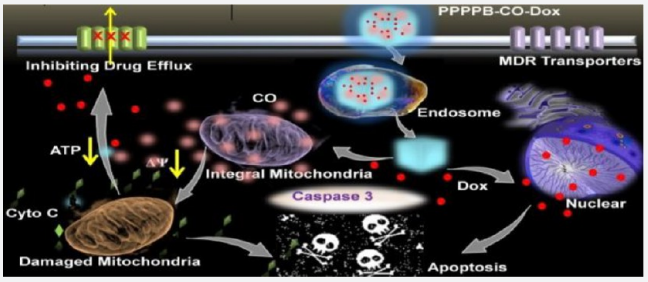

INTRODUCTION

Cancer is the most malignant disease and the first leading cause of mortality in the world.[1−3] While numerous therapeutic modalities have been applied in the clinical setting, chemotherapy still remains as a major anticancer approach.[4−9] However, the occurrence of multidrug resistance (MDR) during the invasion and metastasis of cancer poses a notorious challenge against the success of chemotherapy.[10−13] The mechanism of MDR is often related to the drug efflux by the adenosine triphosphate (ATP)-binding cassette transporters, such as P-glycoprotein (P-gp), which is located on the cell membranes functioning to pump chemodrugs out.[14−18] Thus, various strategies have been designed to overcome MDR, such as utilizing P-gp inhibitors, reducing the nicotinamide adenine dinucleotide (phosphate) (NAD(P)H) and adenosine triphosphate (ATP) to downregulate P-gp expression,[19] targeting anticancer drugs to the mitochondria,[20] and silencing the expression of P-gp proteins using RNA interference.[17,21,22] While these approaches could overcome the MDR to some extent, they displayed intrinsic shortcomings, such as the poor specificity and the high toxicity of P-gp-inhibiting molecules, the complicated chemical synthesis of mitochondria-targeting molecules, and the low transfection efficiency accompanied by siRNA delivery.[23−25] Thus, an effective and safe chemodrug delivery system that can surmount the MDR is still of urgent demand.

Carbon monoxide (CO), an endogenous gas molecule, has recently attracted great attention as a therapeutic reagent.[26] Controlled CO release in the pathological tissues holds great promise in the improvement of cytoprotection and cytoantioxidants.[27−30] More importantly, CO is found to be an important biological gasotransmitter associated with mitochondria, the key cellular energy factory that produces ATP through oxidative phosphorylation and regulates cellular metabolism.[31−34] The mitochondria are also involved in many cellular signaling pathways, and they can produce reactive oxygen species (ROS) as well as program cell death pathways upon membrane permeabilization.[35−37] Treatment of cancer cells with CO accelerates the mitochondrial respiration, thus leading to metabolic exhaustion and mitochondrial collapse.[38] On the basis of these understandings, we hypothesize that the controlled CO delivery in cancer cells could destroy the mitochondria and induce metabolic exhaustion, thus drastically blocking ATP synthesis in the tumor cells and inhibiting the ATP-related drug efflux to overcome MDR.

Received: March 4, 2019
Published: May 24, 2019

© 2019 American Chemical Society

DOI: 10.1021/acscentsci.9b00216
ACS Cent. Sci. 2019, 5, 1044−1058

Scheme 1. Schematic Illustration of NIR-Light-Controlled CO Delivery That Expedites Metabolic Exhaustion To Surmount MDR and Enable Synergistic Proapoptotic Anticancer Therapy[a]

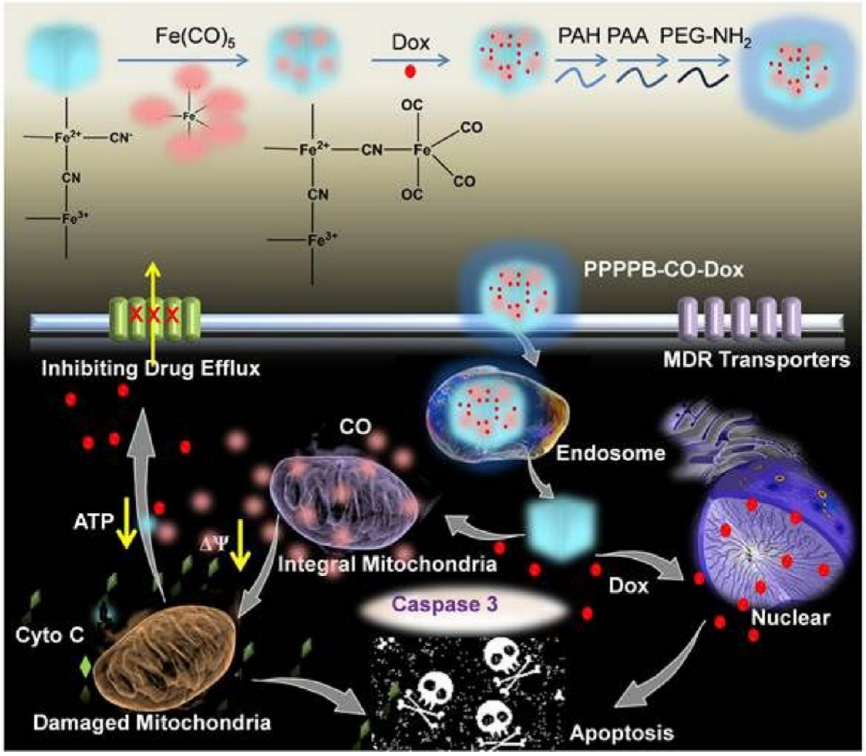

[a]PPPPB−CO−Dox NPs could be accumulated into drug-resistant tumors via the EPR effect, and NIR light irradiation at the tumor site led to nonlethal temperature elevation which caused CO release. CO then expedited mitochondrial metabolic exhaustion, which blocked triphosphate (ATP) synthesis and inhibited ATP-dependent drug efflux to reverse MDR and accordingly potentiate the anticancer efficacy of Dox against Dox-resistant tumors. In the meantime, the CO-mediated mitochondrial exhaustion could upregulate the proapoptotic protein, caspase 3, and generate ROS, thus inducing cellular apoptosis and enabling a synergistic anticancer effect with chemotherapy.

In support of such a hypothesis, we herein developed doxorubicin (Dox)-encapsulated Prussian blue (PB) nanoparticles (NPs), a NIR-light-controlled CO delivery system, to realize tumor mitochondria exhaustion and MDR reversal. These NPs possessed a well-defined core−corona structure, wherein the mesoporous PB core could provoke a photothermal effect and encapsulate Dox in its pores. Pentacarbonyl iron ($Fe(CO)_5$) as a CO producer was coupled to PB via coordination bonding that could be cleaved at a nonlethally high temperature (42 °C) to release CO. The inorganic PB NPs were unstable in the aqueous solution, and thus, they were surface-decorated with hydrophilic polymers to enhance the aqueous stability. Particularly, the negatively charged PB−CO−Dox NPs were sequentially coated with positively charged poly(allylamine hydrochloride) (PAH) and negatively charged poly(acrylic acid) (PAA) using the layer-by-layer (LBL) technique and were further conjugated with poly(ethylene glycol) amine ($PEG-NH_2$) via amide bond formation between PAA and $PEG-NH_2$, yielding the final PPPPB−CO−Dox NPs. Such a surface coating could also avoid the preleakage of Dox during circulation, and the PEG corona would greatly enhance the serum stability of NPs to prolong blood circulation and promote tumor accumulation via the enhanced permeability and retention (EPR) effect. In the acidic endolysosomes of cancer cells, the surface coating was removed due to damaged electrostatic interactions, thus allowing Dox release. The tumor-site-specific NIR light irradiation led to nonlethal temperature elevation, which induced CO release to expedite mitochondrial exhaustion and cause mitochondrial collapse. The APT-dependent drug efflux would be inhibited, and the drug accumulation in the cancer cells could be greatly enhanced to overcome MDR. In addition, the exhausted mitochondria could generate ROS and upregulate the proapoptotic protein, caspase 3, to induce cellular apoptosis and thus mediate the synergistic anticancer effect with Dox-mediated chemotherapy (Scheme 1).

RESULTS AND DISCUSSION

Preparation and Characterization of PPPPB−CO NPs.

PB NPs were successfully synthesized from kaliumhexacyano ferrat (III) and polyvinylpyrrolidone (PVP) in HCl (0.01 M).[39] The transmission electron microscopy (TEM) image of PB NPs revealed diameters of 110.9 ± 17.2 nm along with a cubic morphology (Figure 1a, Figure S1 and Table S1). PB−CO NPs were then synthesized by coupling pentacarbonyl iron ($Fe(CO)_5$) to PB NPs via the coordination interaction between iron groups (Fe) on PB NPs and cyano (CN) groups (Fe−CN) on $Fe(CO)_5$. Fourier transform infrared (FT-IR) spectroscopy showed a small peak of C═O vibration at 1646 cm^{-1} for PB NPs, which was due to the PVP residues. In comparison, an enhanced C═O vibration intensity (1646 cm^{-1}) was noted for PB−CO NPs when the $Fe^{3+}-NC-Fe^{2+}$ vibration intensity (2086 cm^{-1}) was equal for PB NPs and PB−CO NPs (Figure 1b), demonstrating successful synthesis of PB−CO NPs with coordinated iron carbonyl. The amount of $Fe(CO)_5$ incorporated into the PB NPs was calculated by

DOI: 10.1021/acscentsci.9b00216
ACS Cent. Sci. 2019, 5, 1044−1058

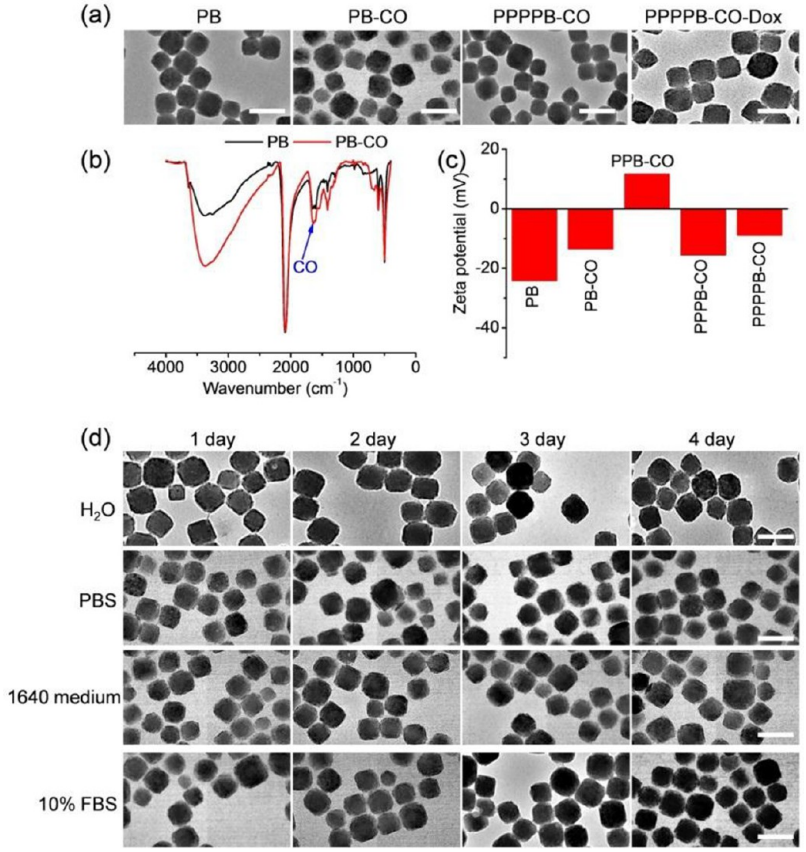

Figure 1. Characterization of NPs. TEM images (a), IR spectra (b), and ζ potentials (c) of different NPs. Scale bar = 200 nm. (d) TEM images of PPPPB−CO NPs after incubation with PBS, H_2O, 1640 medium, and 10% FBS at RT for different time. Scale bar = 200 nm.

determining the Fe content in PB NPs and PB−CO NPs using inductively coupled plasma atomic emission spectroscopy (ICP-AES). The amount of Fe in PB NPs and PB−CO NPs was determined to be 0.453 and 0.403 mg/mg, respectively, and thus, the amount of $Fe(CO)_5$ in PB NPs was calculated to be 0.298 mg/mg, correlating to the maximum CO release amount of 0.213 mg from 1 mg of PB−CO NPs. PB−CO NPs also showed a cubic morphology and diameters of ∼120 nm (Figure 1a and Table S1). To enhance the colloidal stability, the surface of PB−CO NPs was decorated with PEG via the LBL strategy. The negatively charged PB−CO NPs were sequentially coated with poly(allylamine hydrochloride) (PAH) and poly(acrylic acid) (PAA) and ultimately conjugated with PEG_{5k}−NH_2 via the coupling reaction, yielding the PPPPB−CO NPs. The ζ potentials of PB−CO NPs increased from −15 to +12 mV after the PAH coating (PPB−CO NPs) and again decreased to −18 mV after the PAA coating (PPPB−CO NPs), indicating the successful LBL coating (Figure 1c). After conjugation with PEG_{5k}−NH_2, the negative ζ potential changed to −10 mV (PPPPB−CO NPs), which was due to the partial shielding of surface charges by the hydrophilic PEG corona. The PPPPB−CO NPs also revealed a cubic morphology, and they possessed a slightly increased diameter (∼128 nm) compared to PB NPs and PB−CO NPs (Figure 1a and Table S1). Moreover, the PPPPB−CO NPs exhibited the desired colloidal stability in various solutions including H_2O, PBS, 1640 medium, and 10% fetal bovine serum (FBS), after preservation at room temperature (RT) for up to 4 days (Figure 1d).

Light-Mediated Photothermal Effect and Heat-Induced CO Release *In Vitro*. To investigate the photothermal properties of PPPPB−CO NPs, aqueous solutions of PPPPB−CO NPs (10, 20, 50, and 100 μg/mL PB) were irradiated with NIR light (808 nm) at different optical densities (0.3, 0.5, 0.8, and 1 W/cm^2). A concentration- and optical-density-dependent temperature elevation was found for PPPPB−CO NPs under irradiation, while PBS as a control showed negligible photothermal change (Figure 2a−d).

The myoglobin (Mb) assay was then used to determine the thermal-induced CO release from PPPPB−CO NPs.[40,41] After incubation of NPs with deoxy-Mb at 42 °C, the absorption of deoxy-Mb at 557 nm decreased, and the typical peaks of MbCO at 540 and 577 nm appeared (Figure 2e), confirming CO release that converted deoxy-Mb into MbCO. In comparison, when the NPs were incubated with deoxy-Mb at 37 °C, the UV−vis absorption curve did not change. Consistent with the temperature elevation curves described above, notable CO release from the PPPPB−CO NPs was detected after light irradiation (808 nm, 0.5 W/cm^2) for 15 min, as evidenced by the strong absorption peaks of MbCO at 540 and 577 nm (Figure 2f). When the irradiation time was further prolonged to 20 min, the absorption curve remained almost unchanged, indicating that no more CO was released. On the basis of these results, we selected the optical intensity of 0.5 W/cm^2 and irradiation time of 15 min for further evaluations.

The light-induced CO release was also explored by ultrasound (US) imaging using the B mode (Figure 2g and Figure S3). PBS (control) and PPPPB−CO NPs were exposed

DOI: 10.1021/acscentsci.9b00216
ACS Cent. Sci. 2019, 5, 1044−1058

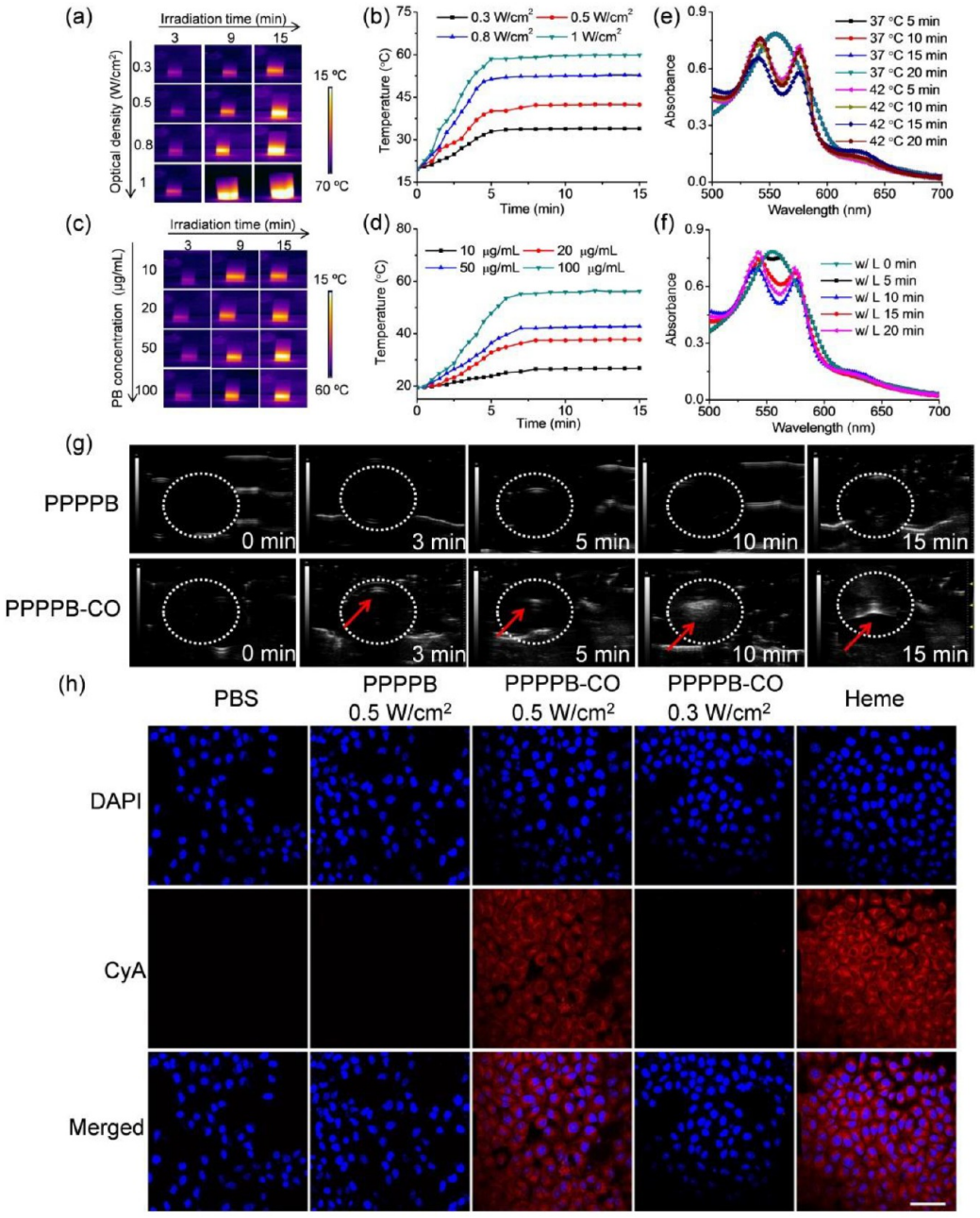

Figure 2. Light-mediated photothermal effect and thermal-induced CO release *in vitro*. Thermal infrared images (a, c) and temperature elevation curves (b, d) of PPPPB−CO NPs following light irradiation (808 nm) at different optical intensities (a, c; 50 μg/mL PB) and different PB concentrations (b, d; 0.5 W/cm^2). (e) UV−vis spectra of deoxy-Mb after incubation with PPPPB−CO NPs at 37 or 42 °C for different times. (f) UV−vis spectra of deoxy-Mb mixed with PPPPB−CO NPs followed by light irradiation (808 nm, 0.5 W/cm^2) for different time. (g) US images of PPPPB NPs and PPPPB−CO NPs after light irradiation (808 nm, 0.5 W/cm^2) for different time. The enhanced echo signal of CO (bright contrast) is indicated by a red arrow. (h) CLSM images of MCF-7/ADR cells stained with the CyA probe for CO detection. Cells were treated with PBS, heme, PPPPB NPs, or PPPPB−CO NPs for 4 h and irradiated (808 nm, 0.5 W/cm^2) for 15 min before the addition of CyA. Scale bar = 20 μm.

to light irradiation (808 nm, 0.5 W/cm^2) for different time (3, 5, 10, and 15 min). No acoustic reflectivity contrast was noted for PBS, while, in contrast, an enhanced echo signal of CO was noted after 3-min irradiation, and it dramatically augmented when the irradiation time was prolonged to 15 min, again substantiating the photothermal-induced CO release.

Then, the CyA probe was used to detect CO release in living cells by confocal laser scanning microscopy (CLSM).[42] MCF-7/ADR cells treated with heme acted as the positive control, because heme can react with endogenous heme oxygenase-1 to produce CO. As shown in Figure 2h, no red fluorescence was detected in cells treated with PBS, PPPPB NPs (irradiated at 0.5 W/cm^2 and 15 min), or PPPPB−CO NPs (irradiated at 0.3 W/cm^2 and 15 min). In contrast, cells incubated with PPPPB−CO NPs followed by irradiation (0.5 W/cm^2, 15 min) showed obvious red intracellular fluorescence, similar to heme-treated cells, which confirmed the effective intracellular CO release upon irradiation at the appropriate optical density and time.

DOI: 10.1021/acscentsci.9b00216
ACS Cent. Sci. 2019, 5, 1044−1058

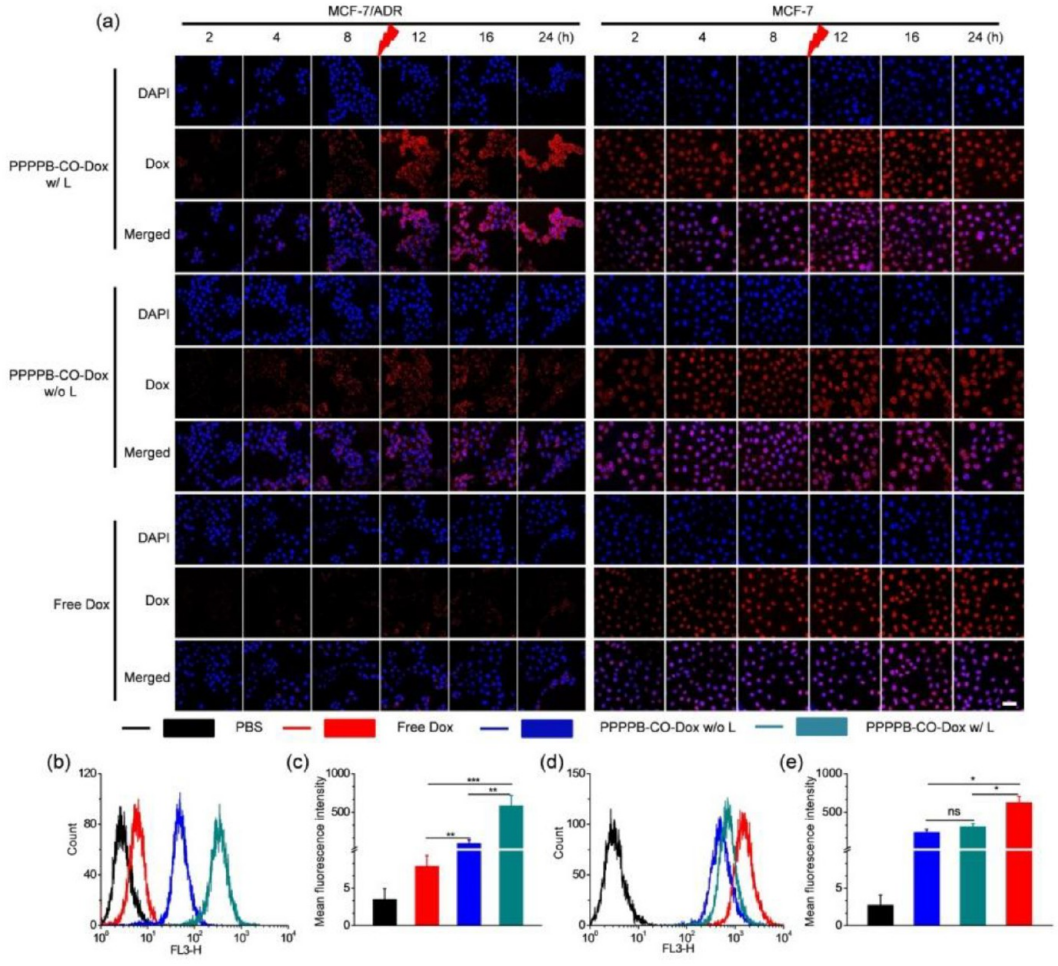

Figure 3. Cellular uptake and CO-enhanced intracellular retention of Dox in resistant cancer cells. (a) CLSM images of MCF-7/ADR and MCF-7 cells following incubation with free Dox or PPPPB−CO−Dox NPs for 2, 4, 8, 12, 16, and 24 h. Cells were irradiated (808 nm, 0.5 W/cm^2) for 15 min after 8-h incubation and were further incubated for 16 h. Scale bar = 15 μm. Flow cytometric analysis of MCF-7/ADR (b, c) and MCF-7 (d, e) cells following 16-h incubation with free Dox or PPPPB−CO−Dox NPs. Cells were irradiated (808 nm, 0.5 W/cm^2) for 15 min after 8-h incubation and were further incubated for 8 h (n = 3). "ns" denotes no significant difference.

Dox Encapsulation and *In Vitro* Release. Prior to drug loading, the pore size of PB NPs was first determined using the Brunauer, Emmett, and Teller (BET) analysis. Figure S2 confirmed the mesoporous structure of the PB NPs, and the pore size was determined to be 5.38 nm, which was large enough to encapsulate Dox (∼1 nm). The loading capacity of Dox was then determined to be 14.5%. The Dox release behavior from PPPPB−CO−Dox NPs was pH-dependent, wherein Dox release was sustained at pH 7.4 but greatly accelerated at pH 5.5, leading to the cumulative release of ∼38% and 85% within 24 h, respectively (Figure S4). Such a pH-dependent drug release profile could be attributed to the LBL coating of the NPs that prevented preleakage of Dox from the inner pores. Under acidic conditions (tumoral endolysosomes), the electrostatic interactions between PAA and PAH were weakened, which led to dissociation of the surface coating and accordingly facilitated Dox release. Such a property could ideally prevent the premature Dox leakage during blood circulation while enable fast drug release in the acidic endolysosomes of tumor cells to impart anticancer efficacy. In addition, Dox shows higher solubility at acidic pH, which also contributed to the accelerated release profile at pH 5.5.

Cellular Uptake and Accumulation of PPPPB−CO−Dox NPs. The cellular uptake of PPPPB−CO−Dox NPs and free Dox in MCF-7 and MCF-7/ADR cells was first observed by CLSM. As shown in Figure 3a, both free Dox and PPPPB−CO−Dox NPs showed strong nuclear fluorescence in MCF-7 cells after incubation for up to 24 h. In obvious contrast, free Dox was hardly visible in MCF-7/ADR cells even after 12-h incubation, indicating chemoresistance of the cells that pumped the free drug out. The PPPPB−CO−Dox NPs also showed a weaker nuclear fluorescence in MCF-7/ADR cells than in MCF-7 cells after incubation for up to 8 h. However, when the MCF-7/ADR cells treated with PPPPB−CO−Dox NPs were irradiated (808 nm, 0.5 W/cm^2, 15 min) at 8 h post incubation, significantly enhanced nuclear fluorescence was observed when the cells were further incubated for up to 8 h (Figure 3a). Such an observation was further supported by the quantitative flow cytometric analyses (Figure 3b−e and Figure S5). In MCF-7 cells, Dox showed a higher accumulation level than PPPPB−CO−Dox NPs, and light irradiation provoked an unappreciable effect on the intracellular level of PPPPB−CO−Dox NPs. In MCF-7/ADR cells, PPPPB−CO−Dox showed a significantly higher cellular level than Dox, and light irradiation of NP-treated cells led to a further increment of the

DOI: 10.1021/acscentsci.9b00216
ACS Cent. Sci. 2019, 5, 1044−1058

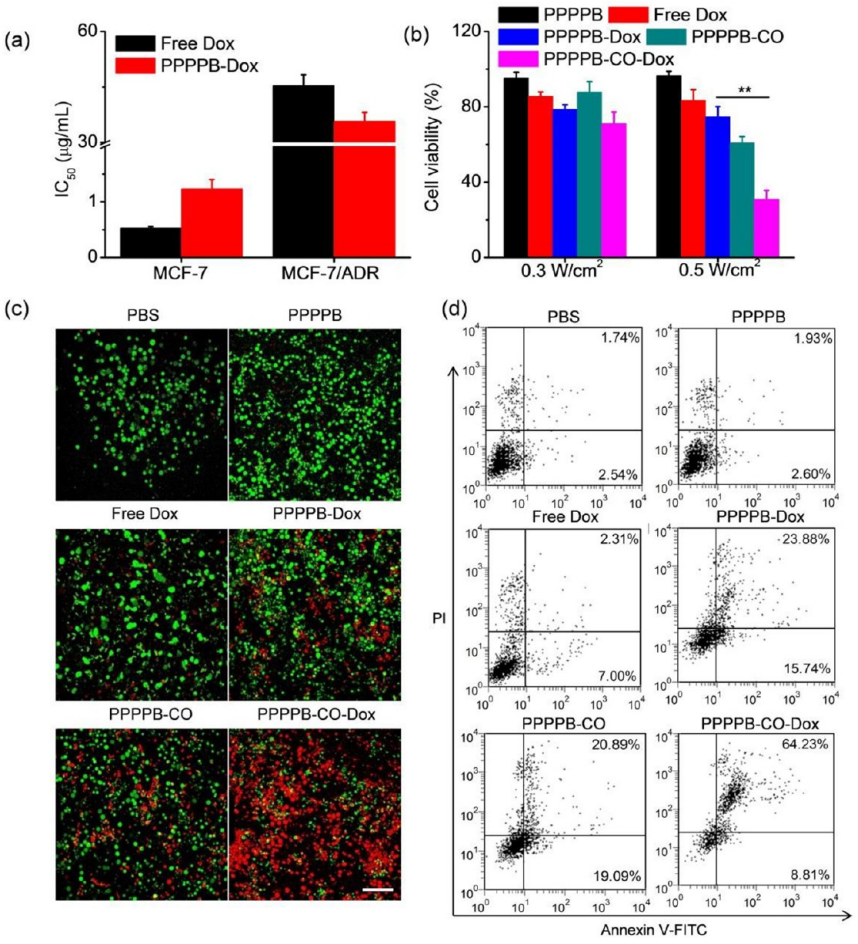

Figure 4. Anticancer efficacy of PPPPB−CO−Dox NPs *in vitro*. (a) IC_{50} values of Dox in MCF-7 and MCF-7/ADR cells. (b) Viability of MCF-7/ADR cells treated with different NPs and irradiated at different optical densities (808 nm, 15 min) (n = 3). (c) CLSM images of MCF-7/ADR cells treated with different NPs and double-stained with calcein-AM (green, live cells) and PI (red, dead cells). Scale bar = 100 μm. (d) Flow cytometric analysis of MCF-7/ADR cells treated with different NPs and stained with Annexin V-FITC/PI. Cells were incubated with different NPs for 8 h at 37 °C, irradiated (808 nm, 0.5 W/cm^2) for 15 min, and further incubated for 48 h before the above assessments.

accumulation level. Taken together, these results indicated the reversal of MDR by the light-released CO molecules that prohibited drug efflux and enhanced intracellular drug accumulation.

***In Vitro* Anticancer Efficacy of PPPPB−CO−Dox NPs.** To determine whether the efficient intracellular accumulation could contribute to MDR reversal, the *in vitro* anticancer efficacies of free Dox and PPPPB−CO−Dox NPs were first assessed in both MCF-7 and MCF-7/ADR cells. As shown in Figure 4a, the cytotoxicity of PPPPB−Dox NPs in MCF-7/ADR cells was notably stronger than free Dox, with IC_{50} values of 32.7 and 45.3 μg/mL, respectively. Such a discrepancy therefore indicated that the NPs could partially inhibit drug resistance, mainly due to the endocytosis pathway of the NPs that prevented direct drug efflux by the P-gp. However, both free Dox and PPPPB−Dox NPs displayed dramatically lower IC_{50} in MCF-7 cells (0.5 and 1.23 μg/mL, respectively), indicating the necessity to enhance the capability of NPs in surmounting MDR. As shown in Figure 4b, after light irradiation at 0.3 W/cm^2, PPPPB−CO NPs showed negligible cytotoxicity, and PPPPB−CO−Dox NPs afforded a toxicity comparable to PPPPB−Dox NPs, which was attributed to the insufficient temperature elevation to release CO. Comparatively, after light irradiation at 0.5 W/cm^2, PPPPB−CO−Dox NPs imparted a greatly enhanced anticancer efficacy with cell viability of only ∼15%, significantly outperforming PPPPB−CO NPs and PPPPB−Dox NPs. It therefore suggested that the chemodrug-resistant cells were resensitized by the NIR-light-generated CO molecules to strengthen the anticancer efficacy.

The CO-assisted anticancer efficacy of Dox against resistant cells was further supported by the calcein-AM and propidium iodide (PI) double-staining assay (Figure 4c). Live cells were stained with calcein-AM to emit green fluorescence, while dead cells were stained with PI to emit red fluorescence. Compared with PPPPB−Dox NPs and PPPPB−CO NPs, cells treated with PPPPB−CO−Dox NPs showed the highest red fluorescence density, indicating extensive cell death. In accordance, MCF-7/ADR cells treated with PPPPB−CO−Dox NPs displayed the highest apoptotic ratio (73.04%) as determined using the Annexin V-FITC/PI assay (Figure 4d), remarkably higher than cells treated with free Dox, PPPPB−CO NPs, or PPPPB−Dox NPs (9.31%, 39.98%, and 39.62%, respectively). These results thus collectively demonstrated the enhanced anticancer efficacy of light-activated PPPPB−CO−Dox NPs against Dox-resistant cancer cells.

CO-Mediated MDR Reversal and Proapoptotic Effect *In Vitro*. The capability of PPPPB−CO−Dox NPs to overcome MDR was then mechanistically probed. Because

DOI: 10.1021/acscentsci.9b00216
ACS Cent. Sci. 2019, 5, 1044−1058

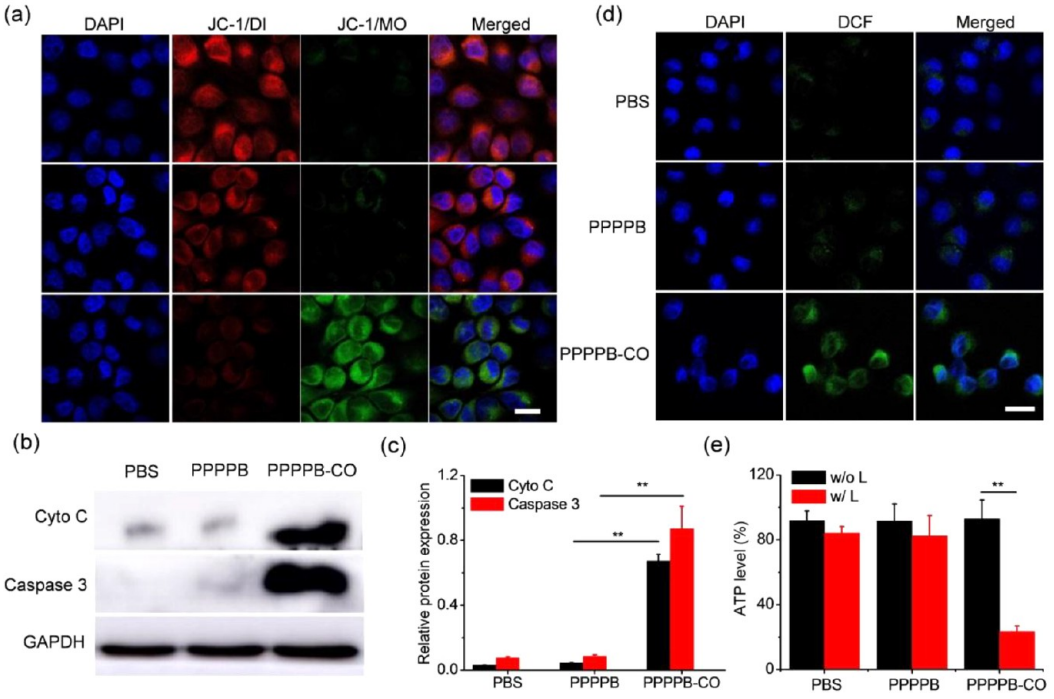

Figure 5. CO-mediated MDR reversal via expedited mitochondrial metabolic exhaustion. (a) Mitochondrial membrane hyperpolarization as detected by the JC-1 probe. Scale bar = 20 μm. (b) Cytoplasmic Cyto C and caspase 3 levels as analyzed by Western blot. (c) Quantified Cyto C and caspase 3 levels according to Western blot images using ImageJ software (n = 3). (d) Intracellular ROS generation as detected by the DCFH-DA probe. Scale bar = 20 μm. (e) Intracellular ATP levels. Cells were incubated with PPPPB NPs or PPPPB−CO NPs for 8 h, irradiated (808 nm, 0.5 W/cm^2) for 15 min, and further incubated for 8 h before the above assessments (n = 3). PBS served as a control.

the MDR mechanism is often closely related to ATP-dependent drug efflux, blocking the energy supply could serve as an effective approach to overcome MDR. A mitochondrial dye, JC-1, was first used to evaluate the mitochondrial membrane depolarization. When the mitochondrial membrane potential (Ψ_m) is high, JC-1 aggregates into the matrix of mitochondria, forming a polymer (J-aggregate) that emits red fluorescence. When the mitochondrial membrane potential is low, JC-1 fails to aggregate in the mitochondria, and it becomes the JC-1 monomer with green fluorescence. The ratio of red to green fluorescence represents the extent of mitochondrial depolarization.[43] Herein, MCF-7/ADR cells treated with PPPPB−CO−Dox NPs followed by light irradiation showed greatly enhanced green fluorescence intensity yet reduced red fluorescence intensity, indicating a disturbance of the mitochondrial membrane permeability (Figure 5a). As a consequence of the mitochondrial collapse, cytochrome c (Cyto C) release into the cytoplasm was significantly enhanced (Figure 5b,c), and the intracellular ATP level was dramatically diminished (Figure 5e). The ATP concentration was maintained at low levels of 25−35% over 36 h post-light-irradiation, indicating that CO-mediated metabolic exhaustion could last for a long period of time (Figure S6). The mitochondrial collapse would simultaneously lead to the generation of reactive oxygen species (ROS) and afterward cause cell apoptosis. To this end, DCFH-DA, a fluorescent probe for ROS, was used to detect CO-mediated ROS generation. Figure 5d showed that light irradiation of cells treated with PPPPB−CO−Dox NPs notably elevated the cellular ROS level, as evidenced by the cytoplasmic green fluorescence. As a consequence, the cellular level of caspase 3, a proapoptotic enzyme, was enhanced by ∼17-fold (Figure 5b,c), which substantiated the capability of NIR-light-released CO in provoking anticancer apoptosis.

Pharmacokinetics and Biodistribution of NPs. The pharmacokinetics of free Dox and PPPPB−CO−Dox NPs were evaluated in nude mice after iv injection. Compared to free Dox that was rapidly cleared from the circulation, the PPPPB−CO−Dox NPs showed notably prolonged blood circulation, conferring a half-life time ($t_{1/2}$) of 3.04 h (Figure S7). The distribution of NPs was then explored in mice bearing MCF-7/ADR tumors after iv injection. As shown in Figure 6a,b, the accumulation level of PPPPB−CO−Dox NPs in the tumor peaked at 8 h post injection, notably outperforming free Dox due to their prolonged circulation and EPR effect. Thus, the tumors were irradiated (808 nm, 0.5 W/cm^2, 15 min) at this time point. At 8 h post irradiation, the tumoral distribution level of PPPPB−CO−Dox NPs was significantly higher than that without light irradiation (Figure 6a,c), which suggested the enhanced drug enrichment in the tumor tissues that could be attributed to the CO-mediated reduction of drug efflux to prevent tumor clearance.

Light-Mediated Photothermal Effect and Heat-Induced CO Release *In Vivo*. According to the biodistribution results, the photothermal effect of PPPPB−CO−Dox NPs *in vivo* was recorded by an infrared (IR) thermal camera at 8 h post iv injection (5 mg Dox/kg). The temperature of the tumor tissues injected with PPPPB−CO−Dox NPs rapidly increased to 42.2 °C, while a much less significant temperature elevation was noted in PBS-treated tumors (up to 37.1 °C), which demonstrated the photothermal effect of PPPPB−CO NPs *in vivo* that could lead to a nonlethally higher temperature in the tumors to release CO upon NIR light irradiation (Figure 6e). Consistent with the temperature elevation profile, minimal CO generation was noted after light irradiation for 3 min using

DOI: 10.1021/acscentsci.9b00216
ACS Cent. Sci. 2019, 5, 1044−1058

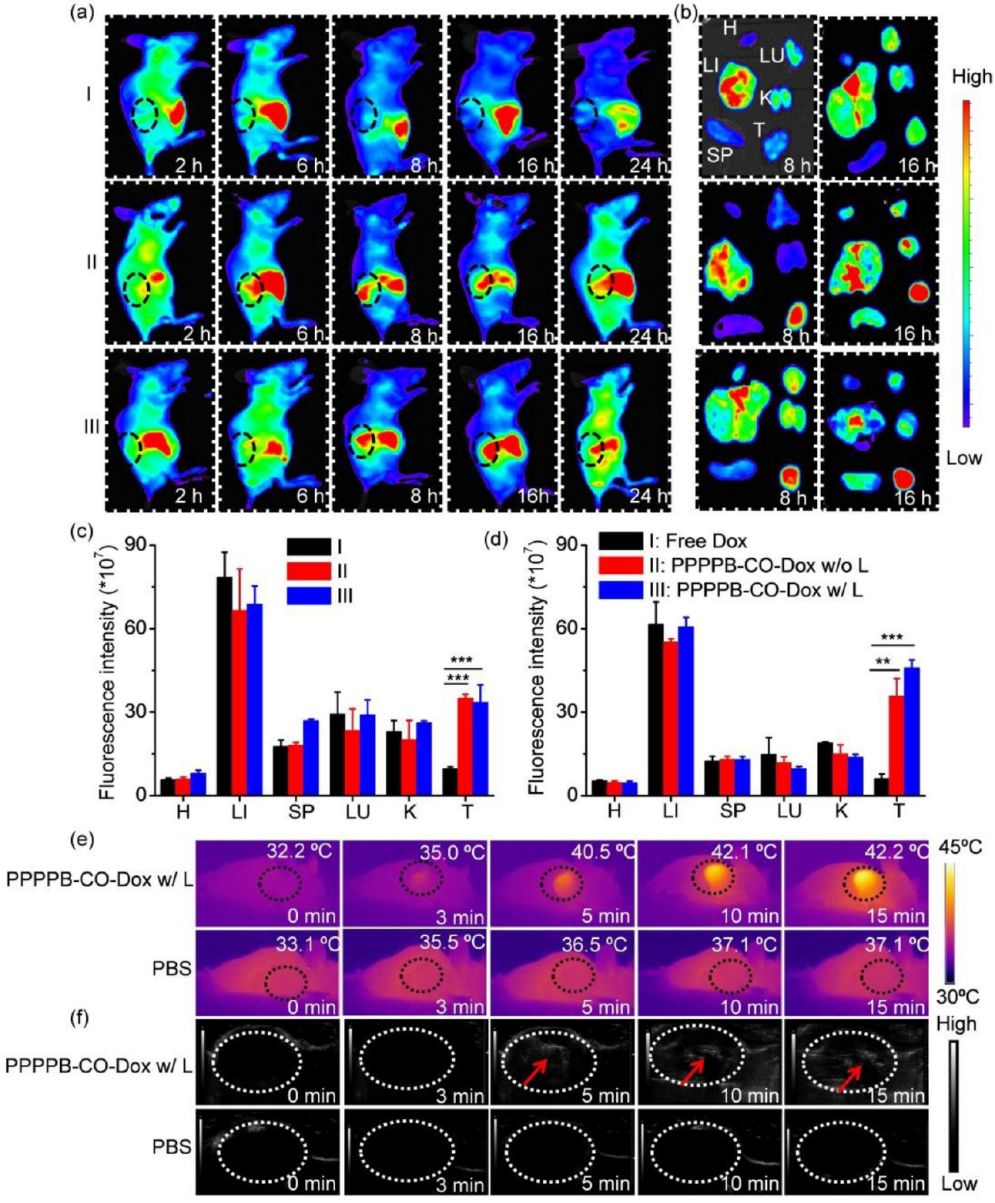

Figure 6. Biodistribution of NPs, NIR-light-mediated photothermal effect, and heat-induced CO release *in vivo*. (a) Fluorescence imaging of MCF-7/ADR tumor-bearing mice at different time intervals post iv injection of PPPPB−CO−Dox NPs and free Dox (5 mg Dox/kg). (b) *Ex vivo* fluorescence imaging of excised tumors and major organs at 8 h post-iv-injection (H, heart; LI, liver; SP, spleen; LU, lung; K, kidney; T, tumor). Biodistribution levels of Dox in tumors and major organs at 8 h (c) and 16 h (d) post iv injection. The tumor site was irradiated (808 nm, 0.5 W/cm^2) for 15 min at 8 h post iv injection in panels a−d. Time-dependent thermal infrared images (e) and US images (f) of tumors after light irradiation (808 nm, 0.5 W/cm^2) for different time. PPPPB−CO−Dox NPs (5 mg Dox/kg) or PBS were iv injected, and tumor tissues were irradiated at 8 h post injection. The enhanced echo signal of CO (bright contrast) is indicated by a red arrow.

US imaging, while further prolonging the irradiation time up to 15 min led to dramatic CO release (Figure 6f and Figure S8).

***In Vivo* Anticancer Efficacy against MCF-7/ADR Xenograft Tumors.** The *in vivo* anticancer efficacy of PPPPB−CO−Dox NPs was evaluated against MCF-7/ADR xenograft tumors. As illustrated in Figure 7a−c, the tumor volumes following iv injection of PBS and PPPPB NPs (with light irradiation) showed the most rapid growth, reaching ∼1000 mm^3 within 21 days. Such a result again demonstrated the nonlethal photothermal effect of PPPPB NPs. PPPPB−Dox NPs showed a slightly higher tumor inhibition level compared to free Dox, consistent with the longer blood circulation time and higher cellular accumulation level of the NPs. Importantly, tumors treated with PPPPB−CO−Dox NPs (with light irradiation) completely stopped growing and even slightly regressed within the 21-day observation period, conferring a tumor growth inhibition rate of 92.7%, remarkably higher than PPPPB−CO NPs (50.3%, with light irradiation) and PPPPB−Dox NPs (64.4%). These results thus evidenced the CO-strengthened anticancer effect of Dox and the cooperative anticancer effect between CO and the chemodrug. Consistent with these findings, tumors treated with PPPPB−CO−Dox NPs showed the most pronounced nuclear condensation and fragmentation in the hematoxylin and eosin (H&E)-staining images that pointed to tumor remission (Figure 7e), and the highest tumor cell apoptotic level was also noted for tumors treated with PPPPB−CO−Dox NPs after TUNEL staining (Figure 7f).

DOI: 10.1021/acscentsci.9b00216
ACS Cent. Sci. 2019, 5, 1044−1058

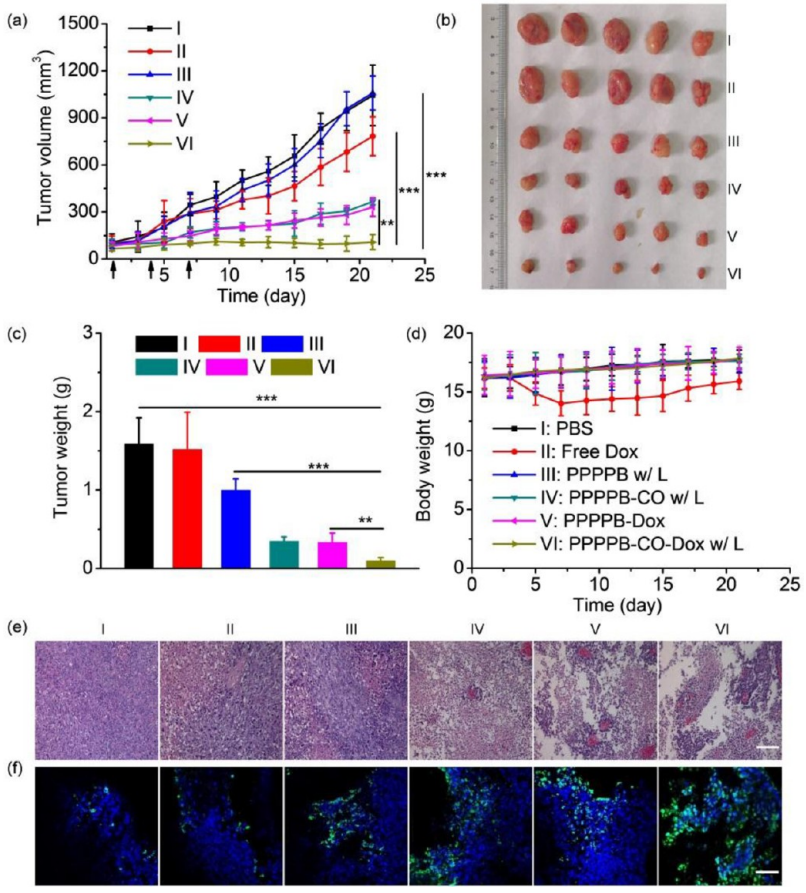

Figure 7. Anticancer efficacy of PPPPB−CO−Dox NPs against MCF-7/ADR tumors. PBS, free Dox, PPPPB NPs, PPPPB−Dox NPs, PPPPB−CO NPs, and PPPPB−CO−Dox NPs were iv injected (5 mg Dox equiv/kg) on day 1, 4, and 7. For PPPPB NPs, PPPPB−CO NPs, and PPPPB−CO−Dox NPs, the tumor sites were irradiated (808 nm, 0.5 W/cm^2, 15 min) at 8 h post injection. Tumor volume progression (a) and body weight change (d) within the 21-day observation period (n = 5). Arrows represented the injection time. Images of excised tumors (b) and tumor weight (c) on day 21 (n = 5). H&E-stained (e) and TUNEL-stained (f) tumor tissues harvested on day 21. Scale bar = 100 μm.

CO-Mediated MDR Reversal *In Vivo*. To evaluate the capability of PPPPB−CO−Dox NPs in reversing MDR *in vivo*, nude mice bearing the MCF-7/ADR tumor were iv injected with the NPs or free ICG [instead of the free Dox because of the limited detection wavelength (750−960 nm) of the PA imaging system and the strong absorbance of ICG at 808 nm]. As revealed by PA imaging, the PA signals (808 nm) from ICG were low and almost constant throughout the entire observation period (Figure 8a). Comparatively, slightly higher PA signals were noted for PPPPB−CO−Dox NPs, possibly due to adequate accumulation of NPs in the tumor tissues. Importantly, a dramatic enhancement of PA signals was noted at 8 h post light irradiation of PPPPB−CO−Dox NP-treated tumors. In accordance with the PA imaging results, CLSM images of tumor sections showed obviously increased intracellular Dox fluorescence intensity after light irradiation of tumors treated with PPPPB−CO−Dox NPs (Figure 8b, Figures S9 and S10). While the majority of Dox was localized in the cytoplasm for PPPPB−CO−Dox NPs at 8 h post irradiation, it was noted that a large amount of Dox was distributed in the nuclei at 16 h post irradiation, indicating translocation of Dox into the nuclei to impart the anticancer efficacy (Figure S10). Such an observation was further supported by the quantitative flow cytometry analyses, wherein light-irradiated, PPPPB−CO−Dox NP-treated tumor cells showed the highest uptake percentage and cellular fluorescence intensity (Figure 8c,d and Figure S11). In addition, both immunostaining and Western blot analyses revealed that MCF-7/ADR tumors treated with PPPPB−CO−Dox NPs followed by light irradiation exhibited notably reduced P-gp levels as compared to those treated with PBS or PPPPB−Dox NPs without light irradiation (no CO release) (Figure S12). It thus indicated that CO could also downregulate the P-gp expression to contribute to the MDR reversal, which may be attributed to the depletion of energy supply for P-gp expression as a result of CO-mediated mitochondrial exhaustion. These results thus collectively evidenced the capability of NIR-light-generated CO to reverse MDR and enhance tumor cell accumulation of chemodrug *in vivo*.

Biocompatibility Analyses. In addition to the therapeutic potency, biosafety is another important requirement for drug delivery systems. Thus, the systemic toxicity of PPPPB−CO−Dox NPs was explored in 4T1 tumor-bearing BALB/c mice following iv injection and tumor-site-specific light irradiation. The blood oxygen saturation (SPO_2) and pulse rate (PR) of mice remained almost constant (Figure S13), indicating that the regional CO release in tumor tissues did not provoke systemic poisoning within our experimental dosages. Hematological and biochemical analyses also showed a lack of abnormality after iv injection of PPPPB−CO−Dox NPs (Figures S14 and S15). In the above efficacy study in MCF-7/ADR tumor-bearing mice, severe weight loss (over 10%) was

DOI: 10.1021/acscentsci.9b00216
ACS Cent. Sci. 2019, 5, 1044−1058

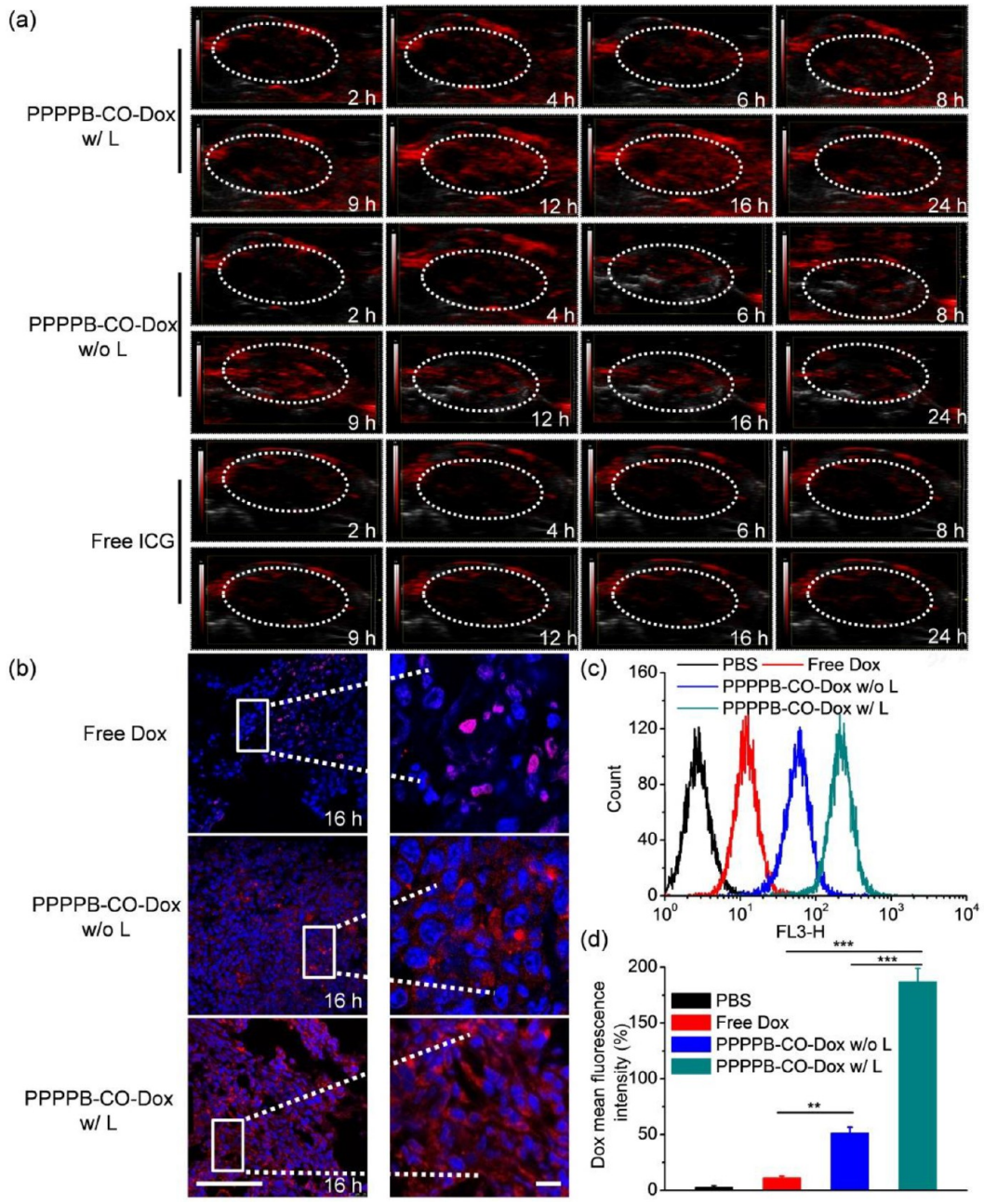

Figure 8. CO-mediated reversal of MDR *in vivo*. (a) PA imaging of MCF-7/ADR tumors at different time intervals post iv injection of free ICG or PPPPB−CO−Dox NPs. Free ICG instead of Dox was used due to the limited detection wavelength (750−960 nm) of the PA imaging system and the strong absorbance of ICG at 808 nm. (b) CLSM images of MCF-7/ADR tumor sections harvested at 16 h post iv injection of free Dox or PPPPB−CO−Dox NPs. Cell nuclei were stained with DAPI. Scale bar = 100 μm. (c, d) Flow cytometric analysis of the accumulation levels of Dox and PPPPB−CO−Dox NPs in tumor cells at 16 h post iv injection (n = 3). In all the assessments, MCF-7/ADR tumor-bearing mice were iv injected with free ICG (or free Dox, 5 mg/kg) or PPPPB−CO−Dox NPs (5 mg Dox/kg), and the tumor sites were irradiated (808 nm, 0.5 W/cm^2, 15 min) at 8 h post injection.

only observed for free Dox (Figure 7d), and a histological assessment revealed apparent cardiac damages including myocardial fibril loss and neutrophil infiltration only in free-Dox-treated mice (Figure S16), indicating the serious side effect of free Dox along with the desired biosafety of the NPs. Taken together, these results demonstrated that the PPPPB−CO−Dox NPs not only can overcome MDR to provoke potent anticancer efficacy, but also displayed the desired biosafety which would conform their promising applications toward anticancer therapy.

CONCLUSION

In summary, a CO and Dox codelivery nanosystem was developed to surmount MDR resistance via regulation of mitochondrial metabolism. The PPPPB−CO−Dox NPs can release CO upon NIR light irradiation, and the released CO can expedite mitochondrial exhaustion to inhibit adenosine triphosphate (ATP) synthesis, thus increasing Dox accumulation in resistant cancer cells to potentiate the anticancer efficacy. In addition, the exhausted mitochondria can upregulate proapoptotic protein, caspase 3, and generate

DOI: 10.1021/acscentsci.9b00216
ACS Cent. Sci. 2019, 5, 1044−1058

ROS to induce cellular apoptosis, thereby provoking synergistic anticancer potency with the chemodrug. To the best of our knowledge, this is the first time that the MDR has been overcome via NIR-light-controlled CO delivery, and this study provides an important addition to the existing approaches in combating chemodrug-resistant tumors.

MATERIALS AND METHODS

Materials. Red prussiate ($K_3[Fe(CN)_6]$), palladium chloride ($PdCl_2$), polyvinylpyrrolidone (PVP), and 1-(3-(dimethylamino) propyl)-3-ethylcarbodiimide hydrochloride (EDC) were purchased from Energy Chemical (Shanghai, China). PEG−NH_2 (M_w = 5 kDa) was obtained from Biomatrik Inc. (Beijing, China). Polyacrylic acid (PAA, M_w = 1.8 kDa), poly(allylamine hydrochloride) (PAH, M_w = 15 kDa), and pentacarbonyl iron ($Fe(CO)_5$) were obtained from Xin Ding Pengfei Technology Development Co., Ltd. (Beijing, China). Doxorubicin (Dox) was purchased from J&K (Shanghai, China). The cytoplasm/mitochondria fractionation kit, mitochondrial membrane potential assay kit (with JC-1), ATP assay kit, ROS assay kit, Annexin V-FITC/PI kit, and live/dead cell double-staining kit were purchased from Beyotime (Shanghai, China) and used according to the protocols provided by the manufacturers. No unexpected or unusually high safety hazards were encountered herein.

Cells. 4T1 (mouse mammary carcinoma) and MCF-7 (human breast adenocarcinoma) cells were purchased from the American Type Culture Collection (ATCC). MCF-7/ADR (P-gp overexpressing human carcinoma cell line, doxorubicin resistant) cells were kindly gifted by Prof. Zhiyuan Zhong's lab in Soochow University. 4T1 Cells were cultured in 1640 medium (Gibco, Grand Island, NY) containing 10% FBS. MCF-7 cells were cultured in DMEM (Gibco, Grand Island, NY) containing 10% fetal bovine serum (FBS). MCF-7/ADR cells were cultured in 1640 medium containing 10% FBS and 50 ng Dox/mL.

Animals. Female BALB/c mice (6−8 week old, 18−20 g) and nude mice (6−8 week old, 16−18 g) were purchased from Shanghai Slaccas Experimental Animal Co., Ltd. (Shanghai, China) and were housed in an SPF room. The animal experimental protocols were performed in strict accordance with the NIH guidelines for the care and use of laboratory animals (NIH Publication 85-23 Rev. 1985) and were approved by the Institutional Animal Care and Use Committee, Soochow University.

Instrumentation. Zeta potential of the NPs was measured by a Malvern Zetasizer (Nanosizer, Malvern, UK). Transmission electron microscopy (TEM, FEI Tecnai F20, acceleration voltage = 200 kV, Jeol) was used to observe the size and morphology of NPs. Fourier transform infrared spectroscopy (FT-IR) (Thermo Fisher, Nicolet iS50) was used to confirm the structure of NPs. The 808 nm laser (Beijing Hai Te Technology Co., Ltd., Beijing, China) was used to irradiate the NPs. The photothermal effect of NPs was monitored by a digital thermometer equipped with a thermocouple probe (MultiTex Corp, Mumbai). The ultraviolet−visible (UV−vis) spectra were recorded on a Lambda 750 UV−vis−NIR spectrophotometer (Shimadzu UV-2450). Ultrasound (US) imaging was performed on a photoacoustic (PA) imaging system (FujiFilm VisualSonics Inc.) with the B mode. The pulse oximeter (RocSea, Shanghai, China) was used to detect the pulse rate (PR) and blood oxygen saturation (SpO_2) of mice. Confocal laser scanning microscopy (CLSM) (TCS SP5, Leica) was used to observe the cellular uptake of NPs. Fluorescence-activated cell sorting (FACS) (BD Biosciences, Oxford, UK) was used to quantitatively evaluate the cellular uptake of NPs. Live animal imaging was performed on the Maestro *in vivo* optical imaging system (Cambridge Research and Instrumentation, Inc.). The Fe content in NPs was measured by inductively coupled plasma atomic emission spectroscopy (ICP-AES) (Aurora, M90). The pore size of NPs was measured by a Brunauer, Emmett, and Teller (BET) analyzer (Quantachrome, IM6).

Synthesis and Characterization of Mesoporous Prussian Blue Nanoparticles (PB NPs). PB NPs were prepared as described before.[39] Briefly, solutions of $K_3[Fe(CN)_6$ (200 mg in 0.01 M HCl, 60 mL) and PVP (6 g in 0.01 M HCl, 60 mL) were mixed and heated at 80 °C. After 24 h, the solution turned blue and was further stirred for another 0.5 h at RT. Acetone (120 mL) was added into the solution, and PB NPs were obtained by centrifugation (14 000 rpm, 5 min) and washing with ethanol (3 × 40 mL). The structure of PB NPs was characterized by DLS, TEM, and FT-IR.

Synthesis and Characterization of Iron Carbonyl-Modified PB NPs (PB−CO NPs). Briefly, PB NPs (5 mg/mL in ethanol, 1 mL) and $Fe(CO)_5$ (50 mg/mL in ethanol, 10 mL) were mixed and mildly stirred at 25 °C for 24 h. PB−CO NPs were obtained by centrifugation (14 000 rpm, 5 min) and washing with ethanol (3 × 40 mL). The structure of PB−CO NPs was characterized by DLS, TEM, and FT-IR.

Synthesis of PAH/PAA/PEG-Conjugated PB−CO NPs (PPPPB−CO NPs). Firstly, PB−CO NPs (1 mg/mL PB in water, 2 mL) was added dropwise into a PAH solution (4 mg/mL in water, 4 mL) under stirring. After the mixture was stirred at 25 °C for 4 h, PAH-coated PB−CO NPs (PPB−CO NPs) were obtained by centrifugation (14 000 rpm, 5 min) and washing with water (3 × 40 mL). Secondly, the obtained PPB−CO NPs (dispersed in water, 4 mL) were added dropwise into a PAA solution (4 mg/mL in water, 1 mL) under stirring. After the mixture was stirred at 25 °C for 4 h, PAA-coated PB−CO NPs (PPPB−CO NPs) were obtained by centrifugation (14 000 rpm, 5 min) and washing with water (3 × 40 mL). Lastly, the mixture of PEG−NH_2 (30 mg) and EDC (15 mg) was added into the obtained PPPB−CO NPs (dispersed in water, 5 mL), and the mixture was stirred overnight. PPPPB−CO NPs were then obtained by centrifugation (14 000 rpm, 5 min) and washing with water (3 × 40 mL).[44] The structure of PPPPB−CO NPs was characterized by DLS and TEM. The size of the NPs after incubation with various solutions including H_2O, PBS, 1640 medium, and 10% FBS for different times at RT was monitored by TEM to evaluate the colloidal stability.

Preparation and Characterization of Dox-Loaded PPPPB−CO NPs (PPPPB−CO−Dox NPs). Dox (10 mg in water, 1 mL) and PB−CO NPs (3 mg in water, 9 mL) were mixed together and stirred at room temperature for 24 h in the dark.[45] PB−CO−Dox NPs were obtained by centrifugation (14 000 rpm, 5 min) at 4 °C. The PB−CO−Dox NPs were then sequentially coated with PAH, PAA, and PEG−NH_2 using the LBL technique as described above. The structure of PPPPB−CO−Dox NPs was characterized by DLS and TEM.

All supernatants during the formation of PPPPB−CO−Dox NPs were collected. The amount of Dox in the supernatant was monitored by spectrofluorimetry (λ_{ex} = 480 nm, λ_{em} = 585 nm). The drug loading contents (DLC) of Dox in the

DOI: 10.1021/acscentsci.9b00216
ACS Cent. Sci. 2019, 5, 1044−1058

PPPPB−CO−Dox NPs were calculated according to the following formula:

$$\text{DLC (wt \%)} = \frac{\text{weight of total drug} - \text{weight of drug in the supernatant}}{\text{weight of NPs} + \text{weight of total drug} - \text{weight of drug in the supernant}} \times 100\%$$

***In Vitro* Dox Release.** The PPPPB−CO−Dox NPs (containing 2.5 mg of Dox) were suspended in PBS (pH 7.4 or 5.5, 25 mL) and kept in a shaking incubator at 37 °C. At predetermined time points, aliquots (1 mL) were taken out and centrifuged at 14 000 rpm for 5 min. An equal volume of PBS was added into the release medium which was further incubated at 37 °C. The Dox concentration in the supernatant was determined by spectrofluorimetry as described above, and the cumulative drug release was calculated.

***In Vitro* Photothermal Effect.** PPPPB−CO NPs solutions at various concentrations (10, 20, 50, and 100 μg/mL PB) were exposed to an 808 nm NIR laser at an optical density of 0.5 W/cm^2 for different time, and the temperature change was measured by a digital thermometer and recorded by an infrared thermal camera. Alternatively, PPPPB−CO NPs (50 μg/mL PB) were irradiated (808 nm) at different optical densities (0.3, 0.5, 0.8, and 1 W/cm^2) for different time before monitoring of the temperature change.

Detection of CO Release by the Myoglobin (Mb) Assay. The Mb assay was used to determine the thermal-induced CO release from PPPPB−CO NPs based on the difference of deoxy-myoglobin (deoxy-Mb) and carbon monoxy-myoglobin (Mb-CO) in the UV−vis spectra.[40,41] First, a fresh solution of deoxy-Mb was prepared by mixing sodium dithionite (0.1% in PBS, 1 mL) and Mb (66 μM in PBS, 5 mL) under a nitrogen atmosphere and stirring at RT for 0.5 h. PPPPB−CO NPs bubbled with nitrogen for 0.5 h were added to the deoxy-Mb solution at the final concentration of 50 μg/mL PB. After incubation at 37 or 42 °C for different time, the UV−vis spectra were recorded.

Light-induced CO release from PPPPB−CO NPs was monitored similarly, wherein the mixture of deoxy-Mb and PPPB−CO NPs was irradiated (808 nm, 0.5 W/cm^2) for different time before recording of the UV−vis spectra.

Detection of CO Release by US Imaging. PPPPB−CO NPs (2 mg/mL PB) were filled into a PE tube, positioned in a 3% agar specimen, and irradiated (808 nm, 0.5 W/cm^2) for different times. US imaging was performed before and directly after irradiation.

Detection of Intracellular CO Release by the CyA Probe. An NIR fluorescence turn-on probe (CyA) was synthesized and used to detect CO release according to a reported method.[42] MCF-7/ADR cells were seeded on a culture dish (d = 1.5 cm) at 2 × 10^6 cells and cultured for 24 h. The medium was replaced by fresh medium, into which heme (100 μM), PPPPB NPs (50 μg/mL PB), or PPPPB−CO NPs (50 μg/mL PB, 15.16 μg/mL CO donor) were added. After 8 h, cells were irradiated (808 nm, 0.3 or 0.5 W/cm^2) for 15 min, and then, the probe solution (CyA and $PdCl_2$, 20 μM) was added. After incubation for another 0.5 h, cells were washed with PBS, stained with Hoechst 33258, and observed by CLSM.

Cellular Uptake and Intracellular Distribution of NPs. MCF-7 or MCF-7/ADR cells were seeded on 24-well plates (2 × 10^5 cells/well) and cultured for 24 h. The medium was replaced with fresh medium, into which free Dox or PPPPB−CO−Dox NPs were added at the final Dox concentration of 5 μg/mL (50 μg/mL PB, 15.16 μg/mL CO donor). After incubation for different time, cells were fixed with 4% paraformaldehyde, stained with DAPI (5 μg/mL), and observed by CLSM. The cells treated with PPPPB−CO−Dox NPs were irradiated (808 nm, 0.5 W/cm^2) for 15 min after 8-h incubation with cells.

To quantify the cellular uptake level, cells incubated with Dox or PPPPB−CO−Dox NPs for 8 and 16 h as described above were collected, resuspended in PBS, and subjected to flow cytometry analysis.

Detection of Mitochondrial Hyperpolarization and ROS Production Induced by CO. MCF-7/ADR cells were seeded on 24-well plates (2 × 10^5 cells/well) and cultured for 24 h. The medium was replaced by fresh medium containing PPPPB NPs or PPPPB−CO NPs (50 μg/mL PB, 15.16 μg/mL CO donor), and after incubation for 8 h, cells were irradiated (808 nm, 0.5 W/cm^2) for 15 min. After 8 h, the mitochondrial membrane potential and intracellular ROS level were explored by CLSM observation using the mitochondrial membrane potential assay kit and reactive oxygen species assay kit, respectively. Cells treated with PBS served as the control.

Determination of Cytoplasmic Cyto C, Intracellular Caspase 3, and ATP Levels. MCF-7/ADR cells were seeded on 6-well plates (2 × 10^6 cells/well) and cultured for 24 h. The medium was replaced by fresh medium containing PPPPB NPs or PPPPB−CO NPs (50 μg/mL PB, 15.16 μg/mL CO donor), and after incubation for 8 h, cells were irradiated (808 nm, 0.5 W/cm^2) for 15 min. After being cultured for another 8 h, the cytosol was collected using a cytoplasm/mitochondria fractionation kit, and the intracellular Cyto C and caspase 3 levels were determined using the Western blot analysis.[46] The intracellular ATP level was determined using the ATP assay kit. Cells treated with PBS served as the control.

***In Vitro* Anticancer Efficacy.** The half-maximal inhibitory concentrations (IC_{50}) of Dox in MCF-7/ADR and MCF-7 cells were determined using the MTT assay. Cells were seeded on 96-well plates (10^4 cells/well) and cultured for 24 h. The culture medium was replaced by fresh medium containing PPPPB−Dox NPs or free Dox at various Dox concentrations. After incubation for 48 h, the cell viability was determined by the MTT assay, and the IC_{50} of Dox was calculated according to reported method.[47] Then, the anticancer efficacies of NPs (PPPPB, PPPPB−Dox, PPPPB−CO, and PPPPB−CO−Dox) were further investigated. MCF-7/ADR cells in 96-well plates were incubated with free Dox or various NPs at 5 μg Dox equiv/mL for 8 h, irradiated (808 nm, 0.3 or 0.5 W/cm^2) for 15 min, and further incubated for 48 h before the MTT assay.

A live/dead double-staining assay was adopted to assess the cytotoxicity. MCF-7/ADR cells were seeded on 24-well plates (2 × 10^5 cells/well), cultured for 24 h, treated with free Dox or various NPs at 5 μg Dox equiv/mL (50 μg/mL PB, 15.16 μg/mL CO donor) for 8 h, irradiated (808 nm, 0.5 W/cm^2) for 15 min, and further incubated for 48 h. Cells were then stained with calcein-AM (2 μM, for live cells) and PI (4.5 μM, for dead cells) for 15 min before observation by CLSM.

The cell apoptosis induced by NPs was further evaluated. MCF-7/ADR cells were seeded on 6-well plates (3 × 10^6 cells/well) and treated with Dox or various NPs as described above. Cells were collected, stained using the Annexin V-FITC/PI kit, and subjected to flow cytometry analysis.[48]

Pharmacokinetics and Biodistribution of NPs. For the pharmacokinetics study, BALB/c mice were iv injected with

DOI: 10.1021/acscentsci.9b00216
ACS Cent. Sci. 2019, 5, 1044−1058

PPPPB−CO−Dox NPs or free Dox at 5 mg Dox/kg. At predetermined time intervals, blood (50 μL) was collected from the orbit and mixed with Triton X-100 (1%, 600 μL) and HCl (1% in isopropyl alcohol, 900 μL). After incubation in the dark overnight, the mixture was centrifuged at 1000*g* for 30 min. The concentration of Dox in the supernatant was quantified by spectrofluorimetry (λ_{ex} = 480 nm, λ_{em} = 585 nm). The half-life time ($t_{1/2}$) of free Dox and PPPPB−CO−Dox NPs was calculated according to the reported method.[49]

For the biodistribution study, MCF-7/ADR cells (2×10^6) in PBS (50 μL) were subcutaneously injected into the right flank of female nude mice. When the tumor volume reached ∼100 mm^3, free Dox or PPPPB−CO−Dox NPs were iv injected at 5 mg Dox/kg. The tumor site was irradiated (808 nm, 0.5 W/cm^2) for 15 min at 8 h post injection. Whole animal fluorescence imaging was performed at predetermined time intervals, and tumor tissue or major organs (heart, liver, spleen, lung, kidney) were harvested at 8 or 16 h post injection. *Ex vivo* imaging was performed, and the fluorescence intensity of Dox in each tissue was quantified using a Maestro *in vivo* optical imaging system (Cambridge Research and Instrumentation, Inc.)

Photothermal Effect of NPs *In Vivo*. Nude mice bearing MCF-7/ADR tumors (∼100 mm^3) were iv injected with PPPPB−CO−Dox NPs (5 mg Dox/kg, 25 mg PB/kg), and the tumor site was irradiated (808 nm, 0.5 W/cm^2) for different time at 8 h post injection. PBS was injected as a control. The time-dependent temperature change in tumors was recorded by an infrared thermal camera.

Detection of CO Production in Tumors by US Imaging. Nude mice bearing MCF-7/ADR tumors (∼100 mm^3) were iv injected with PPPPB−CO−Dox NPs (5 mg Dox/kg, 25 mg PB/kg, 7.58 mg CO donor/kg) or PBS. At 8 h post injection, tumor sites were irradiated (808 nm, 0.5 W/cm^2) for different time. US imaging of the tumor sites was performed on a PA imaging system with the B mode.

***In Vivo* Anticancer Efficacy.** Nude mice bearing MCF-7/ADR tumors (∼100 mm^3) were randomly divided into 6 groups (5 mice/group), and they were iv injected with PBS, free Dox, PPPPB NPs, PPPPB−CO NPs, PPPPB−Dox NPs, or PPPPB−CO−Dox NPs at 5 mg Dox equiv/kg (200 μL/injection, 25 mg PB/kg, 7.58 mg CO donor/kg) on day 1, 4, and 7. At 8 h post injection of PPPPB NPs, PPPPB−CO NPs, and PPPPB−CO−Dox NPs, the tumor sites were irradiated (808 nm, 0.5 W/cm^2, 15 min). The tumor size and body weight were measured every other day, and the tumor volume (V) was calculated according to the formula V = tumor length × width^2/2. Mice with tumors larger than 1000 mm^3 were euthanized according to the standard animal protocol. On day 21, mice were sacrificed, and major organs as well as tumors were excised, weighed, imaged, and subjected to hematoxylin and eosin (H&E) staining and TUNEL staining.

***In Vivo* Tumor Cell Internalization of NPs.** Nude mice bearing MCF-7/ADR tumors (∼100 mm^3) were iv injected with PPPPB−CO−Dox NPs (5 mg/kg Dox, 25 mg PB/kg, 7.58 mg CO donor/kg) or free ICG (5 mg/kg). Free ICG instead of free Dox was used due to the limited detection wavelength (750−960 nm) of the PA imaging system and the strong absorbance of ICG at 808 nm.[50,51] At 8 h post injection, the tumor site was irradiated (808 nm, 0.5 W/cm^2) for 15 min. PA imaging was performed at different time (2, 4, 6, 8, 9, 12, 16, and 24 h) post injection.

In a parallel study, nude mice bearing MCF-7/ADR tumors (∼100 mm^3) were iv injected with PPPPB−CO−Dox NPs or free Dox (5 mg Dox/kg, 25 mg PB/kg, 7.58 mg CO donor/kg). At 8 h post injection, the tumor site was irradiated (808 nm, 0.5 W/cm^2) for 15 min. Mice were sacrificed at 8, 16, and 24 h post injection, and tumors were harvested, embedded in OCT, cryosectioned, and stained with DAPI (5 μg/mL) before observation by CLSM.[22]

To quantify the internalization level of NPs by tumor cells *in vivo*, PPPPB−CO−Dox NPs or free Dox was iv injected, and the tumor site was irradiated as described above. The tumor tissues were collected at 8 and 16 h post injection, washed by PBS, cut into pieces, and incubated with hyaluronidase and collagenase (1.5 mg/mL) at 37 °C for 1 h. The mixture was filtered with nylon mesh, and the cells were centrifuged at 1500 rpm for 3 min, resuspended in PBS containing 1% FBS (0.2 mL), and analyzed by flow cytometry.

In a parallel study, the tumors were embedded in OCT, cryosectioned, and subjected to immunofluorescence staining of P-gp. The concentrations of primary antibodies and Cy3-conjugated IgG antibody were 1:200. The P-gp levels in MCF-7/ADR tumors were also determined by Western blot, and the concentrations of primary and second antibodies were both 1:1000. GAPDH was used as a protein loading control.

Biosafety Evaluation. BALB/c mice bearing 4T1 xenograft tumors (∼100 mm^3) were iv injected with PPPPB−CO−Dox NPs (5 mg Dox/kg, 25 mg PB/kg, 7.58 mg CO donor/kg). The tumor site was irradiated (808 nm, 0.5 W/cm^2) for 15 min at 8 h post injection. Mice injected with PBS served as the control. At different time post light irradiation, the blood oxygen saturation (SpO_2) and pulse rate (PR) of mice were determined using a pulse oximeter. The sensor was placed on the foot to record the signal. At 24 h post irradiation, blood was collected, and the hematological assessment was performed on a BC-5380 automatic hematology analyzer (Mindray), including blood cell count (WBC), granulocyte count (GR), lymphocyte count (LY), mononucleus count (MO), granulocyte % (GR%), lymphocyte % (LY%), mononucleus % (MO%), red blood cell count (RBC), hemoglobin (HGB), mean corpuscular volume (MCV), platelet count (PLT), plateletocrit (PCT), and mean platelet volume (MPV). The blood was centrifuged at 12 000 rpm for 10 min, and the supernatant was subjected to a biochemical parameter assessment on a Cobas501 automatic chemistry analyzer (Roche), including uric acid (UA), alanine transaminase (ALT), total protein (TP), total bilirubin (T-Bil), alkaline phosphatase (ALP), aspartate transaminase (AST), creatinine (CREA), blood urea nitrogen (BUN), glucose (Glu), total cholesterol (TC), and creatine kinase (CK).

Statistical Analysis. All data were presented as mean ± SD, and the statistical analysis was performed using the Student's *t*-test. Differences between two groups were judged to be significant at $^*p < 0.05$ and very significant at $^{**}p < 0.01$ and $^{***}p < 0.001$.

■ ASSOCIATED CONTENT

Supporting Information

The Supporting Information is available free of charge on the ACS Publications website at DOI: 10.1021/acscentsci.9b00216.

Additional results for nanoparticle characterization, *in vitro* and *in vivo* studies, accumulated release profiles,

DOI: 10.1021/acscentsci.9b00216
ACS Cent. Sci. 2019, 5, 1044−1058

pharmacokinetics analyses, cell uptake behavior, CLSM images, flow cytometry, and hematology analysis (PDF)

AUTHOR INFORMATION

Corresponding Author

*E-mail: lcyin@suda.edu.cn. Phone: 86-512-65882039.

ORCID

Lichen Yin: 0000-0002-4573-0555

Author Contributions

The manuscript was written through contributions of all authors. All authors have given approval to the final version of the manuscript.

Notes

The authors declare no competing financial interest.

ACKNOWLEDGMENTS

This work was supported by the Ministry of Science and Technology of China (2016YFA0201200), the National Natural Science Foundation of China (51722305, 51573123, and 51873142), 111 project, and Priority Academic Program Development of Jiangsu Higher Education Institutions (PAPD).

REFERENCES

(1) Peer, D.; Karp, J. M.; Hong, S.; Farokhzad, O. C.; Margalit, R.; Langer, R. Nanocarriers as An Emerging Platform for Cancer Therapy. *Nat. Nanotechnol.* **2007**, *2* (12), 751−760.

(2) Li, C. X.; Zhang, Y. F.; Li, Z. M.; Mei, E. C.; Lin, J.; Li, F.; Chen, C. G.; Qing, X. L.; Hou, L. Y.; Xiong, L. L. Light-Responsive Biodegradable Nanorattles for Cancer Theranostics. *Adv. Mater.* **2018**, *30* (8), 1870049.

(3) Carlisle, J. W.; Ramalingam, S. S. A Banner Year for Immunotherapy and Targeted Therapy. *Nat. Rev. Clin. Oncol.* **2019**, *16* (2), 79−80.

(4) Allen, T. M.; Cullis, P. R. Drug Delivery Systems: Entering the Mainstream. *Science* **2004**, *303* (5665), 1818−1822.

(5) Petros, R. A.; DeSimone, J. M. Strategies in the Design of Nanoparticles for Therapeutic Applications. *Nat. Rev. Drug Discovery* **2010**, *9* (8), 615−627.

(6) Lin, J.; Wang, M.; Hu, H.; Yang, X. Y.; Wen, B.; Wang, Z. T.; Jacobson, O.; Song, J. B.; Zhang, G. F.; Niu, G. Multimodal-Imaging-Guided Cancer Phototherapy by Versatile Biomimetic Theranostics with UV and $\hat{I}^3$-Irradiation Protection. *Adv. Mater.* **2016**, *28* (17), 3273−3279.

(7) Guo, X.; Li, D.; Yang, G.; Shi, C.; Tang, Z.; Wang, J.; Zhou, S. Thermo-Triggered Drug Release from Actively Targeting Polymer Micelles. *ACS Appl. Mater. Interfaces* **2014**, *6* (11), 8549−8559.

(8) Kuang, J.; Wen, S.; Yin, J.; Xuan, Z.; Song, H.; Zhao, Y. P.; Tao, J.; Liu, C. J.; He, X. H.; Zhang, X. Z. iRGD-Modified Chemo-Immunotherapeutic Nanoparticles for Enhanced Immunotherapy against Glioblastoma. *Adv. Funct. Mater.* **2018**, *28* (17), 1800025.

(9) Wang, Q.; Cheng, H.; Peng, H.; Zhou, H.; Li, P. Y.; Langer, R. Non-Genetic Engineering of Cells for Drug Delivery and Cell-Based Therapy. *Adv. Drug Delivery Rev.* **2015**, *91*, 125−140.

(10) Robey, R. W.; Pluchino, K. M.; Hall, M. D.; Fojo, A. T.; Bates, S. E.; Gottesman, M. M. Revisiting the Role of ABC Transporters in Multidrug-Resistant Cancer. *Nat. Rev. Cancer* **2018**, *18* (7), 452−464.

(11) Blanco, E.; Shen, H.; Ferrari, M. Principles of Nanoparticle Design for Overcoming Biological Barriers to Drug Delivery. *Nat. Biotechnol.* **2015**, *33* (9), 941−951.

(12) Xue, X.; Hall, M. D.; Zhang, Q.; Wang, P. C.; Gottesman, M. M.; Liang, X. J. Nanoscale Drug Delivery Platforms Overcome Platinum-Based Resistance in Cancer Cells Due to Abnormal Membrane Protein Trafficking. *ACS Nano* **2013**, *7* (12), 10452−10464.

(13) Zhang, C.; Liu, L. H.; Qiu, W. X.; Zhang, Y. H.; Song, W.; Zhang, L.; Wang, S. B.; Zhang, X. Z. A Transformable Chimeric Peptide for Cell Encapsulation to Overcome Multidrug Resistance. *Small* **2018**, *14* (11), 1703321.

(14) Wang, T.; Wang, D.; Yu, H.; Wang, M.; Liu, J.; Feng, B.; Zhou, F.; Yin, Q.; Zhang, Z.; Huang, Y. Intracellularly Acid-Switchable Multifunctional Micelles for Combinational Photo/Chemotherapy of the Drug Resistant Tumor. *ACS Nano* **2016**, *10* (3), 3496−3508.

(15) He, Q. J.; Shi, J. L. MSN Anti-Cancer Nanomedicines: Chemotherapy Enhancement, Overcoming of Drug Resistance, and Metastasis Inhibition. *Adv. Mater.* **2014**, *26* (3), 391−411.

(16) Liu, J.; Li, Q.; Zhang, J.; Huang, L.; Qi, C.; Xu, L.; Liu, X.; Wang, G.; Wang, L.; Wang, Z. Safe and Effective Reversal of Cancer Multidrug Resistance Using Sericin-Coated Mesoporous Silica Nanoparticles for Lysosome-Targeting Delivery in Mice. *Small* **2017**, *13* (9), 1602567.

(17) Ni, Q.; Zhang, F.; Zhang, Y.; Zhu, G.; Wang, Z.; Teng, Z.; Wang, C.; Yung, B. C.; Niu, G.; Lu, G. In Situ shRNA Synthesis on DNA-Polylactide Nanoparticles to Treat Multidrug Resistant Breast Cancer. *Adv. Mater.* **2018**, *30* (10), 1705737.

(18) Cho, S. K.; Pedram, A.; Levin, E. R.; Kwon, Y. J. Acid-Degradable Core−Shell Nanoparticles for Reversed Tamoxifen-Resistance in Breast Cancer by Silencing Manganese Superoxide Dismutase (MnSOD). *Biomaterials* **2013**, *34* (38), 10228−10237.

(19) Wang, B.; Yuan, H. X.; Liu, Z.; Nie, C. Y.; Liu, L. B.; Lv, F. T.; Wang, Y. L.; Wang, S. Cationic Oligo(p-Phenylene Vinylene) Materials for Combating Drug Resistance of Cancer Cells by Light Manipulation. *Adv. Mater.* **2014**, *26* (34), 5986−5990.

(20) Mansoori, B.; Mohammadi, A.; Davudian, S.; Shirjang, S.; Baradaran, B. The Different Mechanisms of Cancer Drug Resistance: A Brief Review. *Adv. Pharm. Bull.* **2017**, *7* (3), 339−348.

(21) Wu, M.; Meng, Q.; Chen, Y.; Zhang, L.; Li, M.; Cai, X.; Li, Y.; Yu, P.; Shi, J. Nanoparticles: Large Pore-Sized Hollow Mesoporous Organosilica for Redox-Responsive Gene Delivery and Synergistic Cancer Chemotherapy. *Adv. Mater.* **2016**, *28* (10), 1963−1969.

(22) Meng, H.; Mai, W. X.; Zhang, H. Y.; Xue, M.; Xia, T.; Lin, S. J.; Wang, X.; Zhao, Y.; Ji, Z. X.; Zink, J. I. Codelivery of An Optimal Drug/siRNA Combination Using Mesoporous Silica Nanoparticles to Overcome Drug Resistance in Breast Cancer *In Vitro* and *In Vivo*. *ACS Nano* **2013**, *7* (2), 994−1005.

(23) Wang, T.; Wang, D.; Liu, J.; Feng, B.; Zhou, F.; Zhang, H.; Zhou, L.; Yin, Q.; Zhang, Z.; Cao, Z. Acidity-Triggered Ligand-Presenting Nanoparticles to Overcome Sequential Drug Delivery Barriers to Tumors. *Nano Lett.* **2017**, *17* (9), 5429−5436.

(24) Zhou, Y.; Huang, F.; Yang, Y.; Wang, P.; Zhang, Z.; Tang, Y.; Shen, Y.; Wang, K. Paraptosis-Inducing Nanomedicine Overcomes Cancer Drug Resistance for a Potent Cancer Therapy. *Small* **2018**, *14* (7), 1702446.

(25) Yao, C.; Wang, P.; Li, X.; Hu, X.; Hou, J.; Wang, L.; Zhang, F. Near-Infrared-Triggered Azobenzene-Liposome/Upconversion Nanoparticle Hybrid Vesicles for Remotely Controlled Drug Delivery to Overcome Cancer Multidrug Resistance. *Adv. Mater.* **2016**, *28* (42), 9341−9348.

(26) Romao, C. C.; Blattler, W. A.; Seixas, J. D.; Bernardes, G. J. L. Developing Drug Molecules for Therapy with Carbon Monoxide. *Chem. Soc. Rev.* **2012**, *41* (9), 3571−3583.

(27) Yao, X. X.; Yang, P.; Jin, Z. K.; Jiang, Q.; Guo, R. R.; Xie, R. H.; He, Q. J.; Yang, W. L. Multifunctional Nanoplatform for Photoacoustic Imaging-Guided Combined Therapy Enhanced by CO Induced Ferroptosis. *Biomaterials* **2019**, *197*, 268−283.

(28) Gullotta, F.; Di, M. A.; Ascenzi, P. Carbon Monoxide: An Unusual Drug. *IUBMB Life* **2012**, *64* (5), 378−386.

(29) Chaves-Ferreira, M.; Albuquerque, I. S.; Dijana, M. V.; Coelho, A. C.; Carvalho, S. M.; Saraiva, L. M.; Romao, C. C.; Bernardes, G. J. L. Spontaneous CO Release from Ru(II)$(CO)_2$-Protein Complexes in Aqueous Solution, Cells, and Mice. *Angew. Chem.* **2015**, *127* (4), 1188−1191.

(30) He, Q.; Kiesewetter, D. O.; Qu, Y.; Fu, X.; Fan, J.; Huang, P.; Liu, Y.; Zhu, G.; Qian, Z. NIR-Responsive On-Demand Release of

DOI: 10.1021/acscentsci.9b00216
ACS Cent. Sci. 2019, 5, 1044−1058

CO from Metal Carbonyl-Caged Graphene Oxide Nanomedicine. *Adv. Mater.* **2015**, *27* (42), 6537−6537.
(31) Lo Iacono, L.; Boczkowski, J.; Zini, R.; Salouage, I.; Berdeaux, A.; Motterlini, R.; Morin, D. A Carbon Monoxide-Releasing Molecule (CORM-3) Uncouples Mitochondrial Respiration and Modulates the Production of Reactive Oxygen Species. *Free Radical Biol. Med.* **2011**, *50* (11), 1556−1564.
(32) Almeida, A. S.; Figueiredo-Pereira, C.; Vieira, H. L. Carbon Monoxide and Mitochondria-Modulation of Cell Metabolism, Redox Response and Cell Death. *Front. Physiol.* **2015**, *6*, 33−39.
(33) Almeida, A. S.; Sonnewald, U.; Alves, P. M.; Vieira, H. L. Carbon Monoxide Improves Neuronal Differentiation and Yield by Increasing the Functioning and Number of Mitochondria. *J. Neurochem.* **2016**, *138* (3), 423−435.
(34) Jang, D. H.; Kelly, M.; Hardy, K.; Lambert, D. S.; Shofer, F. S.; Eckmann, D. M. A Preliminary Study in the Alterations of Mitochondrial Respiration in Patients with Carbon Monoxide Poisoning Measured in Blood Cells. *Clin. Toxicol.* **2017**, *55* (6), 579−584.
(35) Peng, T. I.; Chang, C. J.; Guo, M. J.; Wang, Y. H.; Yu, J. S.; Wu, H. Y.; Jou, M. J. Mitochondrion-Targeted Photosensitizer Enhances the Photodynamic Effect-Induced Mitochondrial Dysfunction and Apoptosis. *Ann. N. Y. Acad. Sci.* **2010**, *1042* (1), 419−428.
(36) Li, M. X.; Shan, J. L.; Wang, D.; He, Y.; Zhou, Q.; Xia, L.; Zeng, L. L.; Li, Z. P.; Wang, G.; Yang, Z. Z. Human Apurinic/Apyrimidinic Endonuclease 1 Translocalizes to Mitochondria after Photodynamic Therapy and Protects Cells from Apoptosis. *Cancer Sci.* **2012**, *103* (5), 882−888.
(37) Guo, R.; Peng, H.; Tian, Y.; Shen, S.; Yang, W. Mitochondria-Targeting Magnetic Composite Nanoparticles for Enhanced Phototherapy of Cancer. *Small* **2016**, *12* (33), 4541−4552.
(38) Wegiel, B.; Gallo, D.; Csizmadia, E.; Harris, C.; Belcher, J.; Vercellotti, G. M.; Penacho, N.; Seth, P.; Sukhatme, V.; Ahmed, A.; et al. Carbon Monoxide Expedites Metabolic Exhaustion to Inhibit Tumor Growth. *Cancer Res.* **2013**, *73* (23), 7009−7021.
(39) Li, W. P.; Su, C. H.; Tsao, L. C.; Chang, C. T.; Hsu, Y. P.; Yeh, C. S. Controllable CO Release Following Near-Infrared Light-Induced Cleavage of Iron Carbonyl Derivatized Prussian Blue Nanoparticles for CO-Assisted Synergistic Treatment. *ACS Nano* **2016**, *10* (12), 11027−11036.
(40) G, U. R.; Axthelm, J.; Hoffmann, P.; Taye, N.; Glaeser, S.; Görls, H.; Hopkins, S. L.; Plass, W.; Neugebauer, U.; Bonnet, S. Co-Registered Molecular Logic Gate with a CO-Releasing Molecule Triggered by Light and Peroxide. *J. Am. Chem. Soc.* **2017**, *139* (14), 4991−4994.
(41) Fujita, K.; Tanaka, Y.; Abe, S.; Ueno, T. A Photoactive Carbon-Monoxide-Releasing Protein Cage for Dose-Regulated Delivery in Living Cells. *Angew. Chem., Int. Ed.* **2016**, *55* (3), 1056−1060.
(42) Feng, W.; Feng, G. A Readily Aavailable Colorimetric and Near-Infrared Fluorescent Turn-On Probe for Detection of Carbon Monoxide in Lliving Cells and Animals. *Sens. Actuators, B* **2018**, *255* (3), 2314−2320.
(43) Zheng, D. W.; Li, B.; Li, C. X.; Xu, L.; Fan, J. X.; Lei, Q.; Zhang, X. Z. Photocatalyzing CO_2 to CO for Enhanced Cancer Therapy. *Adv. Mater.* **2017**, *29* (44), 1703822.
(44) Cheng, L.; Gong, H.; Zhu, W.; Liu, J.; Wang, X.; Liu, G.; Liu, Z. PEGylated Prussian Blue Nanocubes as a Theranostic Agent for Simultaneous Cancer Imaging and Photothermal Therapy. *Biomaterials* **2014**, *35* (37), 9844−9852.
(45) Cai, X. J.; Ma, M.; Wu, M. Y.; Zhang, L. L.; Chen, H. R.; Shi, J. L. A Prussian Blue-Based Core−Shell Hollow-Structured Mesoporous Nanoparticle as a Smart Theranostic Agent with Ultrahigh pH-Responsive Longitudinal Relaxivity. *Adv. Mater.* **2015**, *27* (41), 6536−6536.
(46) Wei, H.; Li, Z. W.; Hu, S. S.; Chen, X.; Cong, X. F. Apoptosis of Mesenchymal Stem Cells Induced by Hydrogen Peroxide Concerns both Endoplasmic Reticulum Stress and Mitochondrial Death Pathway Through Regulation of Caspases, p38 and JNK. *J. Cell. Biochem.* **2010**, *111* (4), 967−978.
(47) Ye, M.; Han, Y.; Tang, J.; Piao, Y.; Liu, X.; Zhou, Z.; Gao, J.; Rao, J.; Shen, Y. A Tumor-Specific Cascade Amplification Drug Release Nanoparticle for Overcoming Multidrug Resistance in Cancers. *Adv. Mater.* **2017**, *29* (38), 1702342.
(48) Yang, Y.; Lu, Y.; Abbaraju, P. L.; Azimi, I.; Lei, C.; Tang, J.; Jambhrunkar, M.; Fu, J.; Zhang, M.; Liu, Y. Stepwise Degradable Nanocarriers Enabled Cascade Delivery for Synergistic Cancer Therapy. *Adv. Funct. Mater.* **2018**, *28* (28), 1800706.
(49) Li, J.; Sun, C.; Tao, W.; Cao, Z.; Qian, H.; Yang, X.; Wang, J. Photoinduced PEG Deshielding from ROS-Sensitive Linkage-Bridged Block Copolymer-Based Nanocarriers for On-Demand Drug Delivery. *Biomaterials* **2018**, *170*, 147−155.
(50) Gong, F.; Cheng, L.; Yang, N.; Jin, Q.; Tian, L.; Wang, M.; Li, Y.; Liu, Z. Bimetallic Oxide MnMoOX Nanorods for In Vivo Photoacoustic Imaging of GSH and Tumor-Specific Photothermal Therapy. *Nano Lett.* **2018**, *18* (9), 6037−6044.
(51) Jiang, Y.; Cui, D.; Fang, Y.; Zhen, X.; Upputuri, P. K.; Pramanik, M.; Ding, D.; Pu, K. Amphiphilic Semiconducting Polymer as Multifunctional Nanocarrier for Fluorescence/Photoacoustic Imaging Guided Chemo-Photothermal Therapy. *Biomaterials* **2017**, *145*, 168−177.

DOI: 10.1021/acscentsci.9b00216
ACS Cent. Sci. 2019, 5, 1044−1058